Atomic-Scale Observation of Lithiation Reaction Front in Nanoscale SnO_2 Materials

Anmin Nie,[†,⊥] Li-Yong Gan,[‡] Yingchun Cheng,[‡] Hasti Asayesh-Ardakani,[†] Qianqian Li,[§] Cezhou Dong,[§] Runzhe Tao,[⊥] Farzad Mashayek,[∥] Hong-Tao Wang,[§] Udo Schwingenschlögl,[‡] Robert F. Klie,[⊥] and Reza S. Yassar[†,⊥,∥,*]

[†]Department of Mechanical Engineering—Engineering Mechanics, Michigan Technological University, 1400 Townsend Drive, Houghton, Michigan 49931, United States, [‡]Department of Physical Science and Engineering, King Abdullah University of Science & Technology, Thuwal, 23955-6900, Kingdom of Saudi Arabia, [§]Institute of Applied Mechanics, Zhejiang University, Hangzhou, 310027, People's Republic of China, [⊥]Department of Physics, University of Illinois at Chicago, Chicago, Illinois 60607, United States, and [∥]Mechanical and Industrial Engineering Department, University of Illinois at Chicago, Chicago, Illinois 60607, United States

ABSTRACT In the present work, taking advantage of aberration-corrected scanning transmission electron microscopy, we show that the dynamic lithiation process of anode materials can be revealed in an unprecedented resolution. Atomically resolved imaging of the lithiation process in SnO_2 nanowires illustrated that the movement, reaction, and generation of $b = [\bar{1}\bar{1}1]$ mixed dislocations leading the lithiated stripes effectively facilitated lithium-ion insertion into the crystalline interior. The geometric phase analysis and density functional theory simulations indicated that lithium ions initial preference to diffuse along the [001] direction in the {200} planes of SnO_2 nanowires introduced the lattice expansion and such dislocation behaviors. At the later stages of lithiation, the Li-induced amorphization of rutile SnO_2 and the formation of crystalline Sn and Li_xSn particles in the Li_2O matrix were observed.

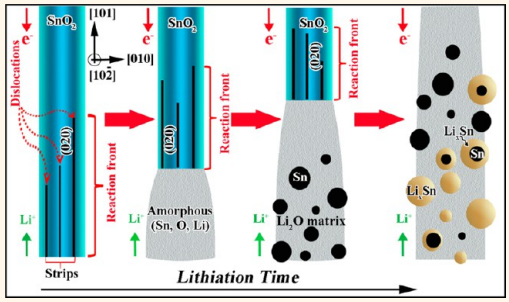

KEYWORDS: lithium-ion batteries · *in situ* STEM · atomic scale · reaction front · tin oxide nanowires

Lithium-ion batteries (LIBs) with excellent energy conversion efficiency and high energy density are increasingly being used in portable electronics and mobile vehicles.[1,2] Development of new high-performance electrode materials for LIBs, especially the anode materials, has been under intense research during the past decade. The design of new electrode materials to a great extent depends on how the lithiation front propagates into the anode material. Therefore, revealing the atomic-scale lithiation mechanism is central to unfolding the performance of electrode materials during the operation of LIBs. Scanning transmission electron microscopy (STEM) with spatial resolution better than 0.1 nm is an indispensible tool that has been used in the battery field for *post-mortem* atomic-scale imaging of lithiated battery materials.[3−7] Moreover, recent progress in aberration-corrected STEM has made it possible to conduct chemical analysis at the atomic scale (resolutions better than 0.35 eV).[8,9] However, the major drawbacks to these earlier studies are the lack of real-time observations while an electrode undergoes structural transition during charging or discharging.

The interest in using *in situ* microscopy for studies of battery materials has seen a dramatic increase since Huang *et al.*[10] and Wang *et al.*[11] reported a prototype nanobattery inside the transmission electron microscope (TEM) using an "open-cell" concept. This cell consists of a single nanowire anode, ionic electrolyte (ionic liquid or solid-state Li_2O), and lithium source ($LiCoO_2$ or lithium metal). With the help of the TEM, the open-cell nanobattery allows direct observation of morphology evolution in real time and provides structure and chemical changing information during the lithiation/delithiation. By using this open-cell nanobattery, the lithiation/delithiation in nanoscale materials, including SnO_2, Si, Ge, Al, ZnO, carbon nanotubes, graphene, and some nanocomposite materials, were investigated.[10,12−24]

* Address correspondence to Reza@mtu.edu.

Received for review April 29, 2013 and accepted June 3, 2013.

Published online June 03, 2013
10.1021/nn402125e

SnO_2 is an ideal anode material for lithiation studies because of multiple lithiation mechanisms.[25−28] Unlike other metal oxide anode materials, the lithiation process of SnO_2 is a combination of intercalation, conversion, and alloying mechanisms. Initially, the Li^+ ion is inserted only into the SnO_2 lattice:

$$SnO_2 + xLi^+ + xe^- \leftrightarrow Li_xSnO_2 \quad (1)$$

Following the intercalation of the lithium ion, an irreversible conversion of the tin oxide to metallic tin occurs:

$$4Li^+ + 4e^- + SnO_2 \rightarrow 2Li_2O + Sn \quad (2)$$

Further lithiation is the reversible alloying reaction:

$$xLi^+ + xe^- + Sn \leftrightarrow Li_xSn\ (0 \le x \le 4.4) \quad (3)$$

Although the recent *in situ* TEM studies[10,14,18,19] on the lithiation process of the SnO_2 nanowire have revealed the morphology evolution and structure changes during the reaction, the *atomistic* mechanisms of dynamical lithiation, at either the early or final stages of lithiation, in SnO_2 nanowires remain unclear. For instance, although the multiple-stripe mechanism[19] was reported during the lithiation of the SnO_2 nanowires, there was no experimental observation of the lithiation stripes dynamical evolution process due to the SnO_2 nanowire immersion inside the liquid electrolyte. Moreover, the author[19] observed the formation of lithiation stripes only when there was a flooding geometry between the SnO_2 nanowire and the electrolyte. However, they did not tell whether the contacting geomtry or other factor is the main determinant of the stripe formation. In addition, there was no direct *in situ* observation of the lithiaion process after the conversion of the tin oxide, though previous *in situ* TEM studies[10,14] indicate the tin metal particles were formed during the lithiation of the SnO_2 nanowires. The shortage of this important part has a significant influence on the understanding of the whole lithation process of the SnO_2 nanowire. Fully addressing these problems critically depends on further atomic level experimental observation and theoritical analysis.

In the present work, taking advantage of *in situ* electrochemistry studies inside an aberration-corrected STEM, the atomistic nature of the dynamic lithiation process of SnO_2 nanowires was revealed using high-angle annular dark field imaging (HAADF). In addition, density functional theory (DFT) simulations were conducted to better understand the experimental results. Our findings show that the lithiation reaction front propagates by long-range Li ion diffusion followed by short-range lithiation of the surrounding matrix. The long-range lithiation process is mediated by the nucleation of dislocations. At the later stages of lithiation, the formation of crystalline Sn and Li_xSn particles in the Li_2O matrix was observed. The findings of this study provide important insight into the physical basis of microstructural evolution, morphological changes, and mechanical degradation in SnO_2 electrodes.

RESULTS AND DISCUSSION

Figure 1a is a scanning electron microscopy (SEM) image of as-synthesized high-density SnO_2 nanowires used in our present experiments. The length of the wires ranged from several to a hundred micrometers. The phases of the SnO_2 nanowires were characterized by X-ray diffraction (XRD) (Figure 1b), which was determined to be a rutile SnO_2 structure (space group: $P4_2/mnm$, lattice constants: $a = 4.737$ Å and $c = 3.186$ Å, JCPDS: 41-1445). The morphology and the structure of the individual pristine SnO_2 nanowires were also characterized by TEM. Figure 1c is a typical TEM image of an individual SnO_2 nanowire demonstrating that the diameter is uniform along the length of the NW. The atomic resolution HAADF and the selected area electron diffraction (SAED) pattern taken with the [010] axis zone (Figure 1d) confirm that the nanowire is a single rutile crystal with the [101] growth direction. The cross-sectional TEM image of the SnO_2 NW (Figure 1e) displays a rectangle cross section by exposing two (020) and two (10$\bar{1}$) surfaces. The corresponding SAED was taken with the [101] zone axis, which is also the SnO_2 nanowires' growth direction. Based on the TEM characterization, the main morphology and the orientation of the SnO_2 nanowires are illustrated in Figure 1f.

The supplementary Movie S1 shows the lithiation of a SnO_2 nanowire with an end-contact geometry. The propagation of the lithiation reaction front along the longitudinal direction of the SnO_2 nanowire can be clearly observed. Upon lithiation, the diameter and length of the nanowire immediately increases. After reaction, the nanowire became amorphous with some embedded dark particles. The speed of reaction in the axial direction was estimated to be about 80 nm/s.

Figure 2 shows the structure and chemistry of the reaction front in a partially lithiated SnO_2 nanowire. The lithiated and unlithiated sections of the nanowire are separated by a dark dotted line in Figure 2a. Interestingly, we observed many dark-contrast stripes emitting toward the unlithiated part of the nanowire as the lithiation reaction front moved forward. It seemed the crystalline-to-amorphous phase transformation of the nanowire started with a long-range diffusion of lithium ions across the crystalline SnO_2.

Figure 2b shows the SAED pattern taken with the [10$\bar{2}$] zone axis from the section of the nanowire marked as B. In the SAED pattern, weak arcs around the {211} diffraction spots can be seen and the {020} diffraction spots are split, which indicates the lithiation-induced polycrystallization and lattice defects. Different contrasts between the dark stripes and the SnO_2 crystalline part are clearly visible by HAADF imaging of area B, as shown in Figure 2c. Since the image intensity in a HAADF image is proportional to the atomic number (Z) (more specifically to $Z^{1.7}$),[29] the bright stripes in Figure 2c should be dominated by the Sn atomic columns,

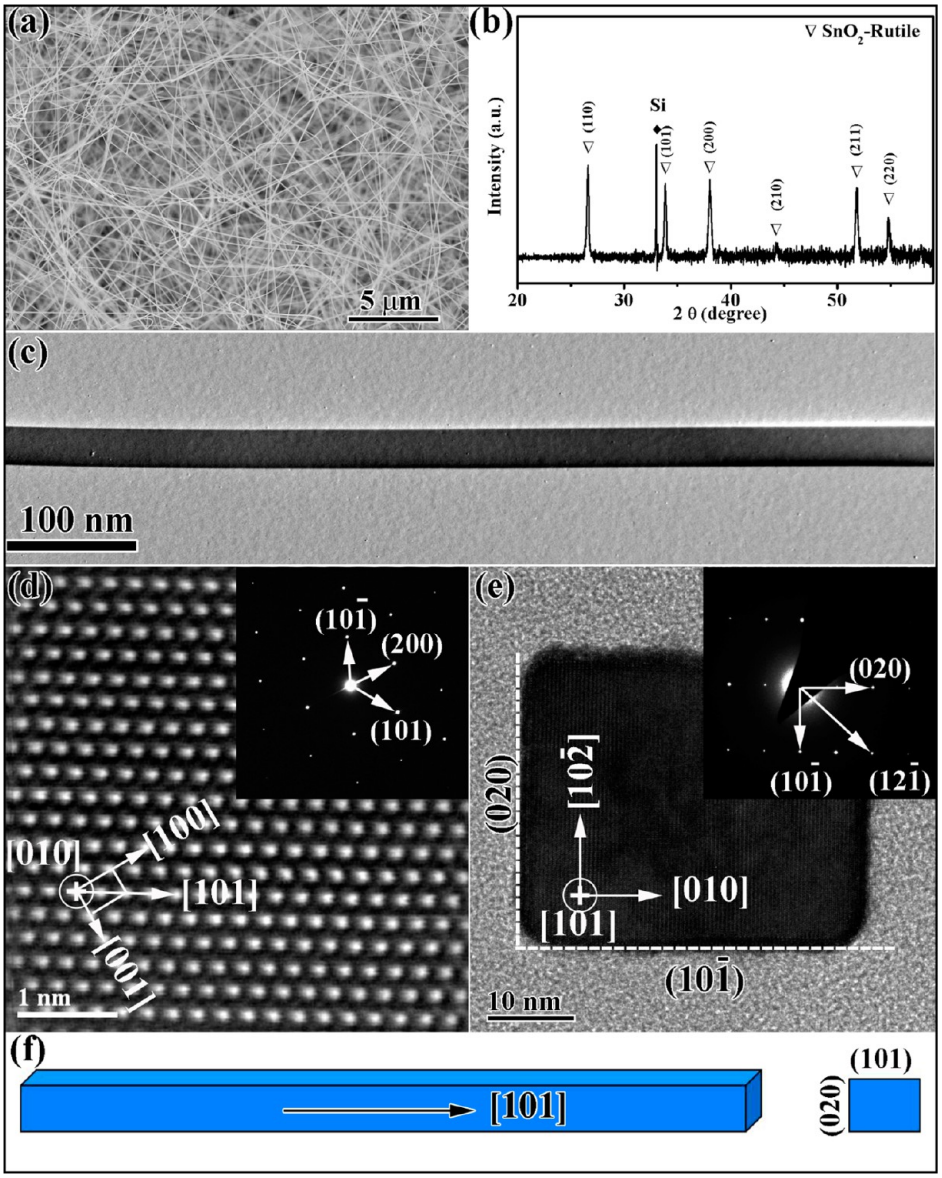

Figure 1. (a) SEM image of the SnO_2 nanowires used in this study. (b) XRD spectrum of SnO_2 nanowires using Cu Kα radiation. (c) Typical TEM image of an individual SnO_2 nanowire. (d) Atomic resolution high-angle annular dark field (HAADF) image from the same nanowire in (a). Inset is the corresponding SAED with the [010] zone axis. (e) Typical cross-sectional HRTEM image of a single SnO_2 nanowire and corresponding SAED with the [101] zone axis. (f) Schematic drawing showing the typical morphology of an individual SnO_2 nanowire.

while the areas with lower image intensity can be correlated to the intercalation of lithium ions and the associated disorder of the tin atomic columns. The lattice inside the stripes became indiscernible, and some stripes (marked in the corner of Figure 2c) seemed to merge with one another. The corresponding bright field image (Figure 2d) provides more direct evidence that the lattice in the dark stripes is almost amorphous. Analysis of electron energy loss spectroscopy (EELS) data (Figure 2f,g) taken from the lithiation stripes indicate that the dark stripes and the adjacent SnO_2 lattice contain lithium. The Li–K edge closely matches that of Li_2O,[10,18] indicating that intercalated Li^+ ions bond with the O atoms of the SnO_2 nanowire. Figure 2e is an atomic resolution HAADF image taken from the area near the tip of a lithiation stripe (area C in Figure 2a). Although, the crystal lattice of the stripe maintains the SnO_2 rutile structure, the EELS analysis (Figure 2h) indicates the presence of Li ions in that area. Consequently, the lithiation of the SnO_2 crystalline nanowires should start with an intercalation mechanism. It is interesting to note that the dark stripes are parallel to the {020} planes (Figure 2b–e), which seems to be the preferred lithium insertion plane.

The tips of the dark stripes that occupied the foremost lithiation positions were further investigated by a series of STEM imaging. Figure 3a–c show atomic resolution HAADF images of the tips of the lithiation stripes in the SnO_2 nanowire viewed along the [10$\bar{2}$] direction. Interestingly, the presence of dislocations at the tip of the stripes was confirmed from the corresponding

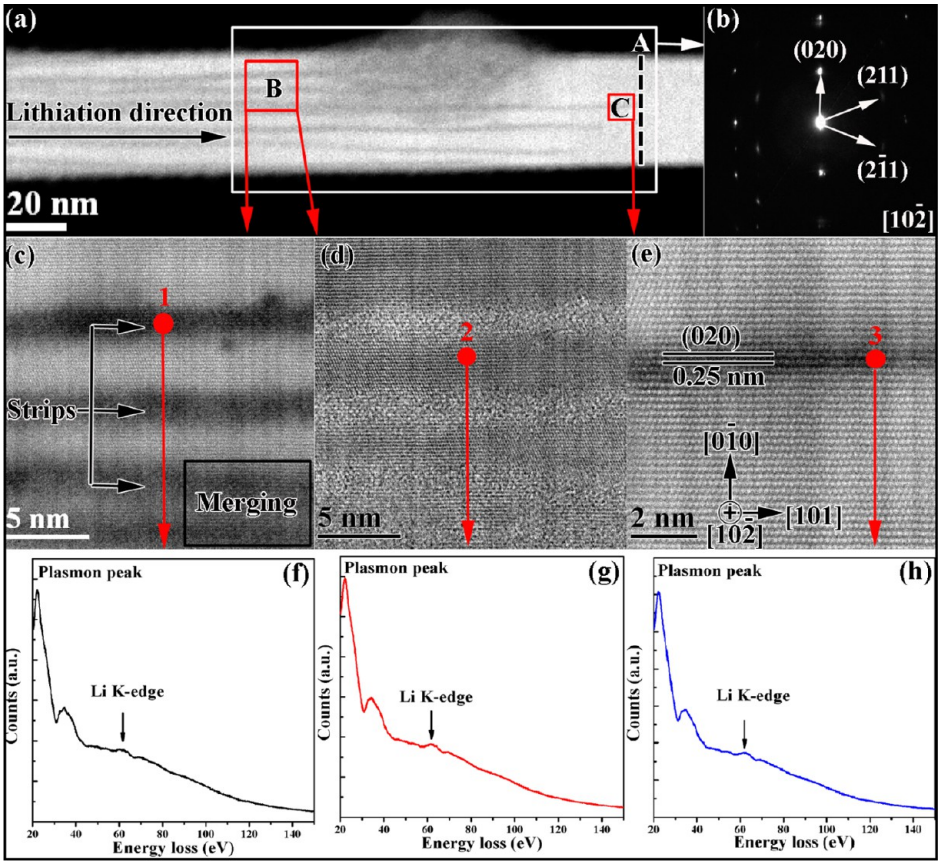

Figure 2. (a) HAADF image taken from the reaction front of a partially lithiated SnO_2 nanowire. (b) Corresponding [10$\bar{2}$] zone axis SAED pattern taken from the area marked as A. (c and d) Higher magnification HAADF and the corresponding bright field images of the area marked as B in (a) showing the lithiation stripes along the SnO_2 nanowire, respectively. (e) Atomic resolution HAADF image taken from the area near the tip of one lithiation stripe. (f−h) EELS spectra taken from the different areas (marked by red spots 1, 2, 3 in STEM images (c−e)) showing the Li−K edge in the SnO_2 nanowire, respectively.

inverse fast-Fourier-transformed (IFFT) images. It should be noted that only the edge component of the dislocation can be determined by HRTEM. By drawing Burgers loops, the edge components of each dislocation in Figure 3a−c were determined to be $b_e = {}^1/_2[1\bar{1}\bar{1}]$, ${}^1/_2[\bar{1}\bar{1}1]$, and ${}^1/_2[\bar{1}\bar{1}1]$, respectively. The unit cell of rutile SnO_2 is primitive tetragonal, although one Sn atom occupies the center position. Thus, the vectors of ${}^1/_2\langle 111\rangle$ do not correspond to the translation vectors of the rutile structure. Since there was no evidence of a stacking fault nearby, it is expected that the dislocations contain screw components (b_s) to make them perfect mixed dislocations. The mixed dislocation with an edge component of $b_e = {}^1/_2[\bar{1}\bar{1}1]$ in the nanowire shown in Figure 3b and Figure 3c seems to dissociate in the (101) plane into two dislocations with edge components $b_e = {}^1/_2[1\bar{1}\bar{1}]$ and $b_e = [\bar{1}01]$, respectively. The former is equal to that of the dislocation in Figure 3a. The latter corresponds to a translation vector of the rutile structure, indicating that one dissociated dislocation is a pure edge dislocation with $b = [\bar{1}01]$. Based on the fact that the energy of the dissociated dislocation is less than the energy of the reactant dislocation, the Burgers vector of the mixed dislocation with the ${}^1/_2[\bar{1}\bar{1}1]$ edge component should be $b = [\bar{1}\bar{1}1]$ by introducing a screw component of ${}^1/_2[\bar{1}\bar{1}1]$. The other mixed dislocation with a ${}^1/_2[1\bar{1}\bar{1}]$ edge component is determined to be $b = [0\bar{1}0]$ by introducing a screw component of ${}^1/_2[\bar{1}\bar{1}1]$. Possible dislocation reactions and elastic stress fields of the dislocations in rutile structures have been systematically investigated by anisotropic elasticity theory and experimental observation.[30−32] It was clarified earlier that the most active slip system in the rutile-structured crystal was $\langle\bar{1}01\rangle\{101\}$,[30] and the dissociation of the $\langle\bar{1}\bar{1}1\rangle\{101\}$-type dislocation into $\langle\bar{1}01\rangle\{101\}$ and $\langle 0\bar{1}0\rangle\{101\}$ was energetically possible.[31] More systematic work is needed to investigate why the foremost lithiation position preferred to form such a $b = [\bar{1}\bar{1}1]$ mixed dislocation. However, it is believed that the lithiation-induced dislocation cores may act as diffusion channels facilitating Li ion insertion into the SnO_2 crystalline interior.[33]

Figure 3(a′−c′) show the ε_{xx} strain field of the HAADF image calculated for a (020) lattice fringe using a 0.8 nm^{-1} mask in the geometric phase analysis.[34,35] The distortion of the lattice was defined with respect to an internal reference area far away from the lithiation stripes and dislocations. The lattice expansion inside

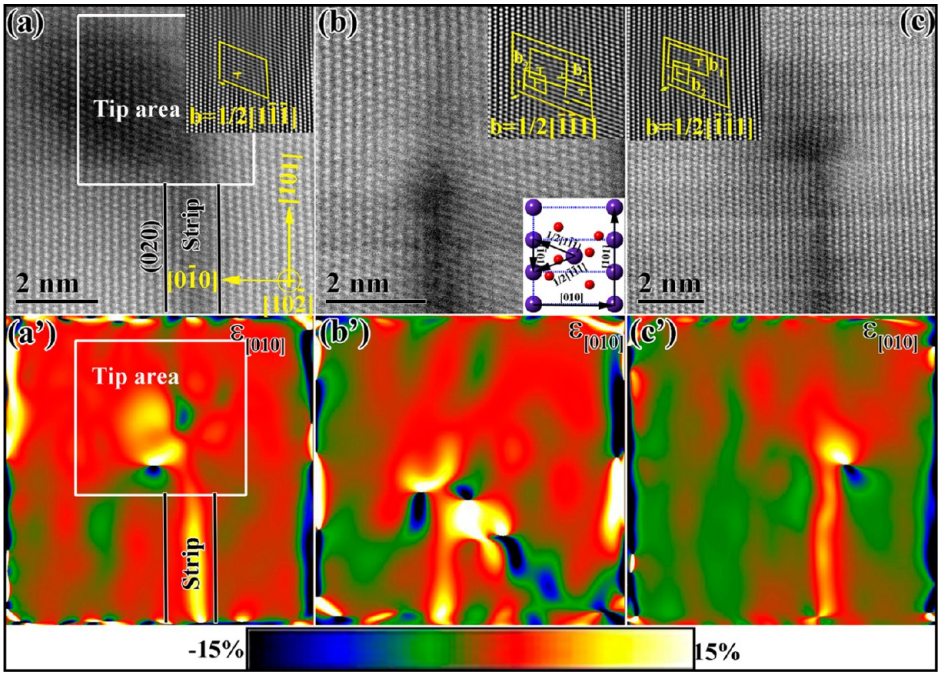

Figure 3. (a−c) Atomic resolution HAADF images of the tips of the lithiation stripes in Figure 2(a) viewed along the [10$\bar{2}$] direction. Top insets are the corresponding inverse fast-Fourier-transformed (IFFT) images showing dislocations with the projected Burgers vector of (a) $b_e = {}^1/_2[1\bar{1}\bar{1}]$, (b) $b_e = {}^1/_2[\bar{1}1\bar{1}]$, and $b_e = {}^1/_2[\bar{1}\bar{1}1]$, respectively. Bottom inset in (b) is the modeled unit cell of SnO_2 viewed along the [10$\bar{2}$] direction. (a′−c′) Corresponding strain maps along the [010] direction. Color range: ±15%.

the lithiation stripes can be clearly seen in the figures. The *d* spacing of (020) (Sn−Sn interatomic distance along [010]) in the lithiation stripes increased by almost 10%. The strain distribution near the cores of the mixed dislocations with $b = [\bar{1}\bar{1}1]$ and $b = [0\bar{1}0]$ was clearly illustrated. Tensile and compressive regions were distinctly separated by the dislocation cores. However, the strain near the $b = [\bar{1}01]$ edge dislocation core was not able to be reflected by the $\varepsilon_{[010]}$ strain map because the stress field of $b = \langle\bar{1}01\rangle$ edge dislocations has a distinct anisotropic effect.[31] Through the above analysis, we note that the initial lithiation of the SnO_2 gives rise to the lattice expansion and dislocations that may facilitate the diffusion of the Li ions into the SnO_2 lattice.

Figure 4a shows a representative HAADF image of a partially lithiated SnO_2 nanowire with a side-contact geometry. Collateral dark stripes and surface defects were formed after the lithiation. The corresponding SAED pattern taken with the [010] zone axis is shown in Figure 4b, which indicates that the lithiation stripes are parallel to the (200) lattice plane. Next, the atomic structural details of slightly (Figure 4c) lithiated stripes were studied by the HAADF imaging. The EELS plot in the inset of Figure 4c confirms the presence of the Li ions in the lithiated stripes. According to the orientation analysis of Figure 4b and c, the Li ion diffusion along the [001] direction in the (200) plane is favored with respect to diffusion taking place along the other direction. Strain mapping (Figure 4d) calculated for the (200) lattice fringe (Figure 4c) indicates that the intercalated Li ions can give rise to a ∼10% lattice expansion in the SnO_2 lattice.

Severely lithiated stripes are also characterized by atomic resolution HAADF, as shown in Figure 4e. The lattice in the upper section of the stripe was almost invisible due to a high degree of Li ion accumulation. In the lower section, one dislocation was identified in the SnO_2 lattice, and its edge component was determined to be $b_e = {}^1/_2[1\bar{1}1]$. It is expected that this dislocation also contains a screw component ${}^1/_2[\bar{1}\bar{1}1]$ or ${}^1/_2[111]$ to make it a perfect dislocation with the Burgers vector of $b = [0\bar{1}0]$ or [101]. Since $\langle\bar{1}01\rangle\{101\}$ is the most active slip system in rutile structures, dislocations with the Burgers vector of $b = [101](10\bar{1})$ are less likely to stay in the lattice near the surface. For this reason, this mixed dislocation is determined to be of $[0\bar{1}0](101)$ slip character, similar to that in Figure 3a.

The activity of the slip systems can explain the formation of surface steps in the lithiated nanowire (Figure 4f). These surface steps should be a result of the cooperative slip events on two conjugate lattice planes by dislocations escaping to the surface. Here, our observation suggests that the lithiation-driven solid-state amorphization of the SnO_2 nanowires is preceded by dislocation plasticity.

To gain better insight into the experimental observation of lithiation in the (200) or (020) plane, the transition barriers along three diffusion paths (*e.g.*, [001], [110], and [010]) in SnO_2 were investigated by

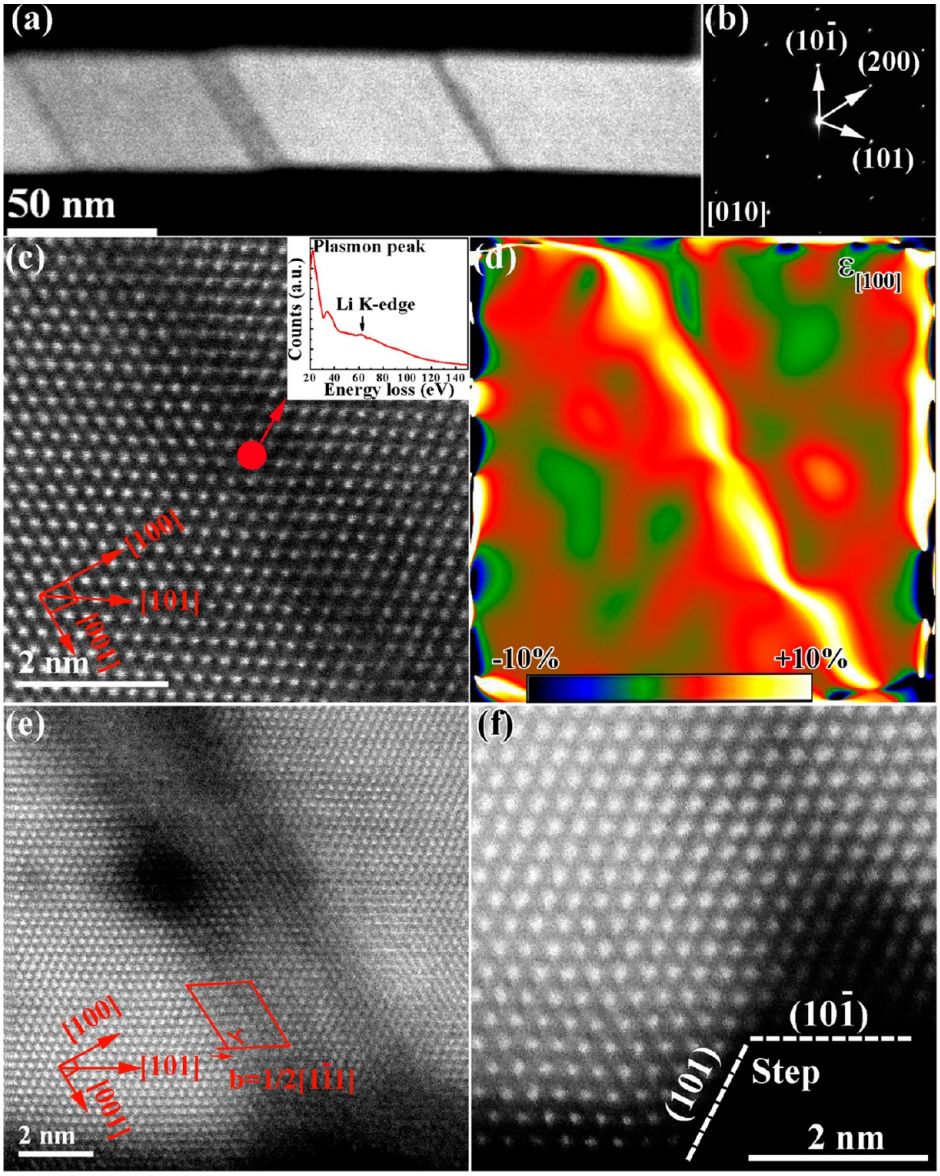

Figure 4. (a) HAADF image of a partially lithiated SnO_2 nanowire with a side-contact geometry. (b) Corresponding SAED pattern taken with the [010] zone axis. (c) Atomic resolution HAADF image taken from a slightly lithiated area in (a). Inset is EELS taken inside the stripe. (d) Strain map with the [100] direction in (c). (e) Atomic resolution HAADF image taken from a relatively severe lithiated area in (a). (f) Atomic resolution HAADF image of a surface step induced by lithiation.

DFT calculations, as shown in Figure 5(a−c). In general, the oxygen-formed octahedra are potentially available to accommodate Li ions for rutile structures.[36] In SnO_2, we find that Li occupation at the off-centered octahedral site (Figure 5(a), Li_1) is the most energetically stable, similar to the case in rutile TiO_2.[36] Along the [001] path, the saddle point is right at the center of the octahedral site (Figure 5(a), Li_1), and the predicted barrier is 0.09 eV, suggesting that Li diffusion along the [001] direction requires very little energy. Due to a large transition barrier (2.08 eV) along the [110] direction, it is difficult for Li to diffuse along this path, as seen in Figure 5(b). The transition barrier along the [010] direction is predicted to be 6.60 eV due to the blocking for Li diffusion along [010] by a strong Sn−Sn bond (Figure5(c)). The above calculation results indicate that Li diffusion along the [001] direction is dominant in rutile SnO_2. This is consistent with our experimental observation in Figure 4 that the lithiation starts with diffusion along [001] in the (200) plane.

To investigate why the lithiation also prefers to proceed along the (020) plane, a lattice expansion model was adopted. The energy cost for lattice expansion in different directions by an intercalated lithium ion was calculated (Figure 5(d)), which provides insight into the most likely direction of expansion by intercalated lithium ions. The expansion is defined as $(l - l_0)/l_0 \times 100\%$, in which l and l_0 indicate the lattice constants in respective expanded and unexpanded unit cells along each direction. It is clear that the energy required to expand the

SnO_2 along the [010] direction is much less than that along [001], [110], and [101], which suggests that the lattice expansion along [010] perpendicular to the (020) lattice plane induced by lithiation is most preferred. This explains our experimental observation in Figures 2 and 3 of the dark lithiation stripes along the (020) planes.

Figure 6a shows a typical TEM image of a fully lithiated SnO_2 nanowire, which is decorated by spherical particles. The particles embedded in the matrix were determined to be Sn or Li_xSn according to the corresponding SAED pattern (inset in Figure 6a). On the basis of the present observation, the overall lithiation characteristics of SnO_2 nanowires are schematically presented in Figure 6b. The structural evolution of an SnO_2 nanowire during the lithiation process occurs *via* the initial lithium-ion long-range diffusion inside the pristine SnO_2 lattice, followed by solid-state amorphization of the nanowire, nucleation of Sn particles, and finally Sn particles alloying into Li_xSn. Multiple stripes parallel to {200} family planes were formed in the reaction front of the SnO_2 nanowire with both end-contact and side-contact geometry. This is different from the observation of Zhong et al.[19] that the stripes appeared only when the nanowire was entirely immersed in the electrolyte. Our result indicates that the formation of the lithiated stripes is a common characteristic of SnO_2 nanowires due to the initial intercalation of the lithium ions in the rutile crystalline structure of the SnO_2 nanowire. It is more accurate to conclude that the imaging of stripes depends on the observation direction (the zone axis and orientation of the SnO_2 nanowire) rather than the contact geometry. Furthermore, at the later stages of lithiation, the Li-induced amorphization of rutile SnO_2 and the formation of crystalline Sn and Li_xSn particles in the Li_2O matrix were observed.

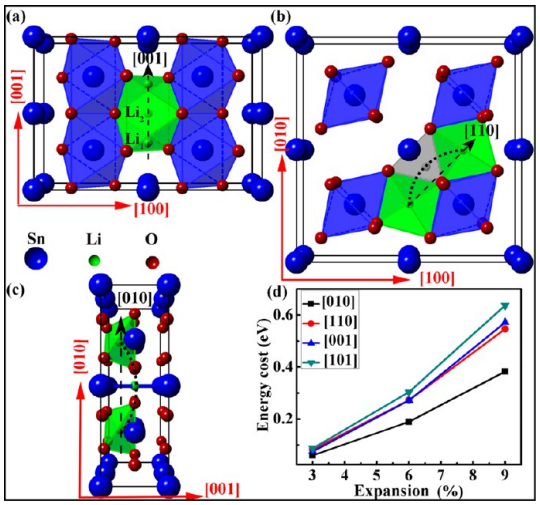

Figure 5. Schematics of lithium diffusion paths (black dashed arrows) between two off-centered octahedral sites in an SnO_2 structure along the [001] (a), [110] (b), and [010] (c) directions. The three energy barriers are 0.09, 2.08, and 6.60 eV, respectively. (a) Li_1 and Li_2 indicate the Li intercalation at the off-centered and the centered octahedral sites, respectively. The gray region in (b) shows Li intercalation at the tetrahedral site. The dotted arcs in (b) and (c) show the diffusion pathways along the [110] and [010] directions. The blue stick connecting the two Sn atoms in (c) indicates a Sn−Sn bond. (d) Energy cost as a function of lattice expansion along the [010], [110], [001], and [101] crystallographic directions.

CONCLUSION

In summary, the atomistic nature of the lithiation mechanism in individual SnO_2 nanowires was fully investigated by *in situ* TEM and complementary DFT simulation. It was found that lithium ions initially preferred to diffuse along the [001] direction in the {200} planes in the SnO_2 crystal. This resulted in a 5−10% lattice expansion and formation of $b = [\bar{1}\bar{1}1]$ mixed dislocations. The movement, reaction, and generation of dislocations effectively facilitated short-range lithium-ion insertion into the crystalline interior.

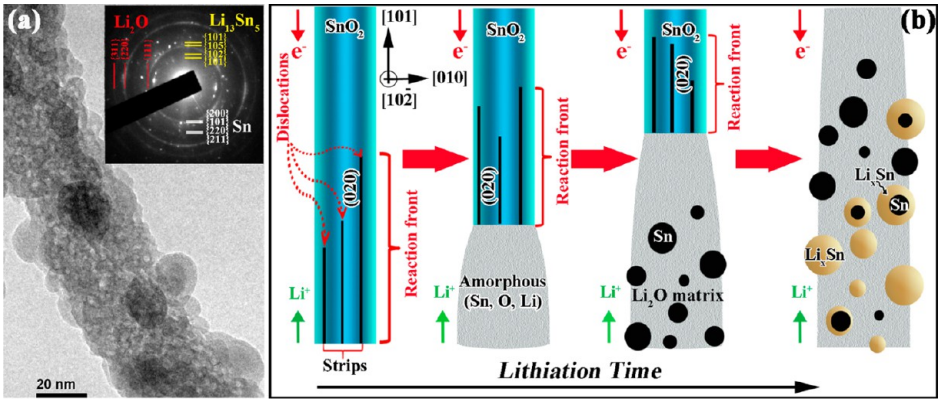

Figure 6. (a) Typical TEM image of a lithiated SnO_2 nanowire and corresponding SAED. (b) Schematic of the lithiation characteristics of the crystalline SnO_2 nanowire featuring the initial lithium-ion long-range diffusion mediated by dislocation activities inside the pristine lattice, followed by solid-state amorphization of the crystalline nanowire, nucleation of Sn particles, and finally the alloying of the Sn particles into Li_xSn.

At later stages of lithiation, Sn and Li_xSn nanoparticles formed in the Li_2O matrix. These results provide a more complete understanding of morphological changes, phase evolution, and mechanical degradation during the lithiation of SnO_2, which could help to develop strategies to build high-performance LIBs.

EXPERIMENTAL DETAILS

The SnO_2 nanowires were grown on Au-coated Si substrates *via* a vapor−liquid−solid mechanism catalyzed by gold nanoparticles as described elsewhere.[37−39] The Sn metal powder was heated in a tube furnace as a source with its container partially covered by the Au-coated Si wafer. The synthesized SnO_2 nanowires were obtained from an hour growth at 800 °C and 4 Torr with Ar flow.

The experiments were carried out inside an aberration-corrected JEOL JEM-ARM200CF STEM equipped with a 200 keV Schottky cold-field emission gun, a HAADF detector, and a postcolumn Gatan Enfina EELS spectrometer. Here, a 22 mrad probe convergence angle was used for all the images and spectra. The HAADF images were acquired using a 90 mrad inner-detector angle, and the EELS spectra were obtained with a 45 mrad collection angle.

The details of the *in situ* Li ion experimental setup is already discussed by the authors in refs 40 and 41 and also by others in refs 13, 17, 21, 42, and 43. Here, Li metal covered with LiO_2 was used as the source of lithium. The SnO_2 nanowires were placed on the negative side of the *in situ* setup and were brought in direct contact with the Li source. When the SnO_2 nanowire electrode is biased to −3 V, Li ions were driven through the solid electrolyte in this experiment. Two contact geometries were investigated in this study. In the first scenario, the free end of the SnO_2 nanowire is in contact with the electrolyte (Li_2O layer) and the lithiation reaction front advances in the axial direction (referred to as an end-contact geometry). The second scenario is that the sides of the SnO_2 nanowire are in contact with the Li_2O layer and the reaction front propagates in the transverse direction (referred to as a side-contact geometry). The lithiation can be stopped at various intermediate stages by retracting the lithium source and electrolyte from the nanowire.

The atomistic calculations were conducted using the Vienna Ab Initio Simulation Package[44] with the frozen-core projector-augmented-wave method.[45] The spin-polarized Perdew, Burke, and Ernzerhof generalized gradient approximation function[46] was employed for the exchange−correlation energy. Specifically, the Sn atom was described by 14 ($4d^{10}5s^25p^2$) valence electrons. The on-site Coulomb correction of the 5d orbital of Sn and the value of $U-J$ = 3.5 eV was used as in ref 47. The energy barriers and minimum energy path of Li diffusion are computed in a ($2 \times 2 \times 3$) supercell containing 24 Sn and 48 O atoms with the climbing image nudged elastic band method.[48] A cutoff energy of 500 eV was employed for the plane-wave expansion, and a $4 \times 4 \times 1$ Gamma-centered *k*-point mesh was used to integrate the Brillouin zone.

Conflict of Interest: The authors declare no competing financial interest.

Acknowledgment. R.S.Y. acknowledges the financial support from the National Science Foundation (Award Nos. CMMI-1200383 and DMR-0820884) and the American Chemical Society Petroleum Research Fund (Award No. 51458-ND10). The acquisition of the UIC JEOL JEM-ARM200CF is supported by an MRI-R^2 grant from the National Science Foundation (Grant No. DMR-0959470). Support from the UIC Research Resources Center is also acknowledged.

Supporting Information Available: Supporting movies (recording the lithiation process of an individual SnO_2 nanowire) as described in the text. This material is available free of charge *via* the Internet at http://pubs.acs.org.

REFERENCES AND NOTES

1. Tarascon, J.; Armand, M. Issues and Challenges Facing Rechargeable Lithium Batteries. *Nature* **2001**, *414*, 359–367.
2. Goodenough, J. B.; Kim, Y. Challenges for Rechargeable Li Batteries. *Chem. Mater.* **2009**, *22*, 587–603.
3. Gu, L.; Zhu, C.; Li, H.; Yu, Y.; Li, C.; Tsukimoto, S.; Maier, J.; Ikuhara, Y. Direct Observation of Lithium Staging in Partially Delithiated $LiFePO_4$ at Atomic Resolution. *J. Am. Chem. Soc.* **2011**, *133*, 4661–4663.
4. Xu, B.; Fell, C. R.; Chi, M.; Meng, Y. S. Identifying Surface Structural Changes in Layered Li-Excess Nickel Manganese Oxides in High Voltage Lithium Ion Batteries: A Joint Experimental and Theoretical Study. *Energy Environ. Sci.* **2011**, *4*, 2223–2233.
5. Ji, L.; Lin, Z.; Alcoutlabi, M.; Zhang, X. Recent Developments in Nanostructured Anode Materials for Rechargeable Llithium-Ion Batteries. *Energy Environ. Sci.* **2011**, *4*, 2682–2699.
6. Lu, X.; Jian, Z.; Fang, Z.; Gu, L.; Hu, Y. S.; Chen, W.; Wang, Z.; Chen, L. Atomic-Scale Investigation on Lithium Storage Mechanism in $TiNb_2O_7$. *Energy Environ. Sci.* **2011**, *4*, 2638–2644.
7. Lu, X.; Zhao, L.; He, X.; Xiao, R.; Gu, L.; Hu, Y. S.; Li, H.; Wang, Z.; Duan, X.; Chen, L.; *et al.* Lithium Storage in $Li_4Ti_5O_{12}$ Spinel: The Full Static Picture From Electron Microscopy. *Adv. Mater.* **2012**, *24*, 3233–3238.
8. Kimoto, K.; Asaka, T.; Nagai, T.; Saito, M.; Matsui, Y.; Ishizuka, K. Element-Selective Imaging of Atomic Columns in a Crystal Using STEM and EELS. *Nature* **2007**, *450*, 702–704.
9. Muller, D.; Kourkoutis, L. F.; Murfitt, M.; Song, J.; Hwang, H.; Silcox, J.; Dellby, N.; Krivanek, O. Atomic-Scale Chemical Imaging of Composition and Bonding by Aberration-Corrected Microscopy. *Science* **2008**, *319*, 1073–1076.
10. Huang, J. Y.; Zhong, L.; Wang, C. M.; Sullivan, J. P.; Xu, W.; Zhang, L. Q.; Mao, S. X.; Hudak, N. S.; Liu, X. H.; Subramanian, A.; *et al. In Situ* Observation of the Electrochemical Lithiation of a Single SnO_2 Nanowire Electrode. *Science* **2010**, *330*, 1515–1520.
11. Wang, C. M.; Xu, W.; Liu, J.; Choi, D.; Arey, B.; Saraf, L. V.; Zhang, J.; Yang, Z.; Thevuthasan, S.; Baer, D. R.; *et al. In Situ* Transmission Electron Microscopy and Spectroscopy Studies of Interfaces in Li Ion Batteries: Challenges and Opportunities. *J. Mater. Res.* **2010**, *25*, 1541–1547.
12. Liu, X. H.; Huang, S.; Picraux, S. T.; Li, J.; Zhu, T.; Huang, J. Y. Reversible Nanopore Formation in Ge Nanowires during Lithiation-Delithiation Cycling: An *In Situ* TEM Study. *Nano Lett.* **2011**, *11*, 3991.
13. Liu, X. H.; Wang, J. W.; Huang, S.; Fan, F.; Huang, X.; Liu, Y.; Krylyuk, S.; Yoo, J.; Dayeh, S. A.; Davydov, A. V.; *et al. In Situ* Atomic-Scale Imaging of Electrochemical Lithiation in Silicon. *Nat. Nanotechnol.* **2012**, *7*, 749–756.
14. Zhang, L. Q.; Liu, X. H.; Perng, Y. C.; Cho, J.; Chang, J. P.; Mao, S. X.; Ye, Z. Z.; Huang, J. Y. Direct Observation of Sn Crystal Growth during the Lithiation and Delithiation Processes of SnO_2 Nanowires. *Micron* **2012**, *43*, 1127–1133.
15. Liu, X. H.; Zhang, L. Q.; Zhong, L.; Liu, Y.; Zheng, H.; Wang, J. W.; Cho, J. H.; Dayeh, S. A.; Picraux, S. T.; Sullivan, J. P.; *et al.* Ultrafast Electrochemical Lithiation of Individual Si Nanowire Anodes. *Nano Lett.* **2011**, *11*, 2251–2258.
16. Liu, Y.; Hudak, N. S.; Huber, D. L.; Limmer, S. J.; Sullivan, J. P.; Huang, J. Y. *In Situ* TEM Observation of Pulverization of Aluminum Nanowires and Evolution of the Thin Surface Al_2O_3 Layers during Lithiation-Delithiation Cycles. *Nano Lett.* **2011**, *11*, 4188–4194.
17. Liu, Y.; Zheng, H.; Liu, X. H.; Huang, S.; Zhu, T.; Wang, J.; Kushima, A.; Hudak, N. S.; Huang, X.; Zhang, S.; *et al.* Lithiation Induced Embrittlement of Multi-Walled Carbon Nanotubes. *ACS Nano* **2011**, *5*, 7245–7253.
18. Wang, C. M.; Xu, W.; Liu, J.; Zhang, J. G.; Saraf, L. V.; Arey, B. W.; Choi, D.; Yang, Z. G.; Xiao, J.; Thevuthasan, S.; *et al. In Situ* Transmission Electron Microscopy Observation of

Microstructure and Phase Evolution in a SnO_2 Nanowire during Lithium Intercalation. *Nano Lett.* **2011**, *11*, 1874–1880.
19. Zhong, L.; Liu, X. H.; Wang, G. F.; Mao, S. X.; Huang, J. Y. Multiple-Stripe Lithiation Mechanism of Individual SnO_2 Nanowires in a Flooding Geometry. *Phys. Rev. Lett.* **2011**, *106*, 248302.
20. Liu, X. H.; Wang, J. W.; Liu, Y.; Zheng, H.; Kushima, A.; Huang, S.; Zhu, T.; Mao, S. X.; Li, J.; Zhang, S.; *et al*. *In Situ* Transmission Electron Microscopy of Electrochemical Lithiation, Delithiation and Deformation of Individual Graphene Nanoribbons. *Carbon* **2012**, *50*, 3836–3844.
21. Liu, X. H.; Zhong, L.; Huang, S.; Mao, S. X.; Zhu, T.; Huang, J. Y. Size Dependent Fracture of Silicon Nanoparticles during Lithiation. *ACS Nano* **2012**, *6*, 1522–1531.
22. McDowell, M. T.; Ryu, I.; Lee, S. W.; Wang, C.; Nix, W. D.; Cui, Y. Studying the Kinetics of Crystalline Silicon Nanoparticle Lithiation with *in Situ* Transmission Electron Microscopy. *Adv. Mater.* **2012**, *24*, 6034–6041.
23. Wang, C.; Li, X.; Wang, Z.; Xu, W.; Liu, J.; Gao, F.; Kovarik, L.; Zhang, J. G.; Howe, J. Y.; Burton, D. J.; *et al*. *In-Situ* TEM Investigation of Congruent Phase Transition and Structural Evolution of Nanostructured Silicon/Carbon Anode for Lithium Ion Batteries. *Nano Lett.* **2012**, *12*, 1624–1632.
24. Yang, H.; Huang, S.; Huang, X.; Fan, F.; Liang, W.; Liu, X. H.; Chen, L. Q.; Huang, J. Y.; Li, J.; Zhu, T.; *et al*. Orientation-Dependent Interfacial Mobility Governs the Anisotropic Swelling in Lithiated Silicon Nanowires. *Nano Lett.* **2012**, *12*, 1953–1958.
25. Zhu, J.; Lu, Z.; Aruna, S.; Aurbach, D.; Gedanken, A. Sonochemical Synthesis of SnO_2 Nanoparticles and Their Preliminary Study as Li Insertion. *Chem. Mater.* **2000**, *12*, 2557–2566.
26. Kim, C.; Noh, M.; Choi, M.; Cho, J.; Park, B. Critical Size of a Nano SnO_2 Electrode for Li-Secondary Battery. *Chem. Mater.* **2005**, *17*, 3297–3301.
27. Park, M. S.; Wang, G. X.; Kang, Y. M.; Wexler, D.; Dou, S. X.; Liu, H. K. Preparation and Electrochemical Properties of SnO_2 Nanowires for Application in Lithium-Ion Batteries. *Angew. Chem.* **2006**, *119*, 764–767.
28. Sensato, F. R.; Gracia, L.; Beltrán, A.; Andrés, J.; Longo, E. Structural and Electronic Properties of Lithiated SnO_2. A Periodic DFT Study. *J. Phys. Chem. C* **2012**, *116*, 16127–16137.
29. Hartel, P.; Rose, H.; Dinges, C. Conditions and Reasons for Incoherent Imaging in STEM. *Ultramicroscopy* **1996**, *63*, 93–114.
30. Suzuki, K.; Ichihara, M.; Takeuchi, S. High-Resolution Electron Microscopy of Lattice Defects in TiO_2 and SnO_2. *Philos. Mag. A* **1991**, *63*, 657–665.
31. Motohashi, Y.; Blanchin, M.; Vicario, E.; Fontaine, G.; Otake, S. Elastic Parameters, Elastic Energy, and Stress Fields of Dislocations in TiO_2 Rutile Crystals. *Phys. Status Solidi A* **1979**, *54*, 355–364.
32. Iwanaga, H.; Egashira, M.; Suzuki, K.; Ichihara, M.; Takeuchi, S. Twins and Dislocations in SnO_2 Whiskers. *Philos. Mag. A* **1988**, *58*, 683–690.
33. Legros, M.; Dehm, G.; Arzt, E.; Balk, T. J. Observation of Giant Diffusivity along Dislocation Cores. *Science* **2008**, *319*, 1646–1649.
34. Hytch, M.; Snoeck, E.; Kilaas, R. Quantitative Measurement of Displacement and Strain Fields from HREM Micrographs. *Ultramicroscopy* **1998**, *74*, 131–146.
35. Hytch, M. J.; Putaux, J. L.; Pénisson, J. M. Measurement of the Displacement Field of Dislocations to 0.03 Å by Electron Microscopy. *Nature* **2003**, *423*, 270–273.
36. Koudriachova, M. V.; Harrison, N. M.; de Leeuw, S. W. Density-Functional Simulations of Lithium Intercalation in Rutile. *Phys. Lett. B* **2002**, *65*, 235423.
37. Pan, Z. W.; Wang, Z. L. Nanobelts of Semiconducting Oxides. *Science* **2001**, *291*, 1947–1949.
38. Nie, A.; Liu, J.; Dong, C.; Wang, H. Electrical Failure Behaviors of Semiconductor Oxide Nanowires. *Nanotechnology* **2011**, *22*, 405703.
39. Nie, A.; Liu, J.; Li, Q.; Cheng, Y.; Dong, C.; Zhou, W.; Wang, P.; Wang, Q.; Yang, Y.; Zhu, Y.; *et al*. Epitaxial TiO_2/SnO_2 Core–Shell Heterostructure by Atomic Layer Deposition. *J. Mater. Chem.* **2012**, *22*, 10665–10671.
40. Ghassemi, H.; Au, M.; Chen, N.; Heiden, P. A.; Yassar, R. S. *In Situ* Electrochemical Lithiation/Delithiation Observation of Individual Amorphous Si Nanorods. *ACS Nano* **2011**, *5*, 7805–7811.
41. Ghassemi, H.; Au, M.; Chen, N.; Heiden, P. A.; Yassar, R. S. Real-Time Observation of Lithium Fibers Growth inside a Nanoscale Lithium-Ion Battery. *Appl. Phys. Lett.* **2011**, *99*, 123113–123113–3.
42. Liu, X. H.; Zheng, H.; Zhong, L.; Huang, S.; Karki, K.; Zhang, L. Q.; Liu, Y.; Kushima, A.; Liang, W. T.; Wang, J. W.; *et al*. Anisotropic Swelling and Fracture of Silicon Nanowires during Lithiation. *Nano Lett.* **2011**, *11*, 3312–3318.
43. Liu, X. H.; Huang, J. Y. *In Situ* TEM Electrochemistry of Anode Materials in Lithium Ion Batteries. *Energy Environ. Sci.* **2011**, *4*, 3844–3860.
44. Kresse, G.; Furthmuller, J. Efficient Iterative Schemes for *ab Initio* Total-Energy Calculations Using a Plane-Wave Basis Set. *Phys. Rev. B* **1996**, *54*, 11169–11186.
45. Blöchl, P. E. Projector Augmented-Wave Method. *Phys. Rev. B* **1994**, *50*, 17953–17979.
46. Perdew, J. P.; Burke, K.; Ernzerhof, M. Generalized Gradient Approximation Made Simple. *Phys. Rev. Lett.* **1996**, *77*, 3865–3868.
47. Singh, A. K.; Janotti, A.; Scheffler, M.; Van de Walle, C. G. Sources of Electrical Conductivity in SnO_2. *Phys. Rev. Lett.* **2008**, *101*, 055502.
48. Henkelman, G.; Uberuaga, B. P.; Jónsson, H. A Climbing Image Nudged Elastic Band Method for Finding Saddle Points and Minimum Energy Paths. *J. Chem. Phys.* **2000**, *113*, 9901.